ORIGINAL PAPER

One-step microwave-assisted solvothermal nano-manufacturing of Ni₂P nanosphere as high-performance supercapacitors

Peng Zhang[1] · Wenxian Wang[2] · Zimin Kou[1] · Jinzhe Li[1] · Tao Wang[1] · Jibao Guo[3]

Abstract

Ni₂P nanospheres were prepared by an ultrafast (120 s), easy, and energy-efficient one-step microwave method. By controlling the reaction conditions and feed ratio, Ni₂P nanospheres with novel nanostructures and ultra-high electrochemical properties were prepared. These nanospheres demonstrated a high specific capacitance of 404.2 F g^{-1} at 1 A g^{-1} and high cycling durability. They maintain 81% of their initial capacity after 2000 cycles at 6 A g^{-1}. The optimum device based on Ni₂P//AC showed an outstanding energy density of 27.2 Wh kg^{-1} and power density of 375 W kg^{-1}. A method that is much faster and much more energy-efficient than other approaches was developed to produce transition metal phosphates without atmosphere protection.

Keywords Microwave-assisted · Solvothermal · Ni₂P · Supercapacitors

Introduction

With the ever-growing energy demand and upgrading of electronic products, the development of highly efficient energy storage systems that are low cost and environmentally friendly has become urgent. Supercapacitors (SCs) and lithium ion batteries (LIBs) are two widely used energy storage devices that possess some advantages, including high safety, high design flexibility, and excellent performance [1–4]. Generally speaking, SCs can address the gap between high-power electrostatic capacitors and high-energy batteries. The electrochemical performance of SCs is markedly dependent on their electrode materials. Typically, carbon materials (activated carbon, carbon fiber, and graphite) are often used as electrodes with long cycle life and high structure stability. However, the disadvantage of carbon materials, such as low capacitance and low energy density, cannot satisfy the harsh demands of new-generation electronic devices [5]. This issue inspired the pursuit of new and safe electrode materials with higher capacitance and energy densities, such as metal oxides [6], metal sulfides [7] and metal phosphides [8]. Among of them, transition metal phosphides (TMPs) that compounded transition metal (Fe [9–11], Ni [12, 13], Co [14, 15], Mo [16], and Sn [17]) with elemental P have attracted much attention owing to their excellent electrochemical performance and high chemical stability [9].

Ni-P compounds (NiP$_y$) are among the promising TMP electrode materials for SCs [18], LIBs [3, 19], and for other applications, such as sodium-ion batteries, electrical catalysis [20], hydrogen evolution reactions, and oxygen evolution reactions [21]. NiP$_y$ can be classified as P-rich phase ($y > 1$) and Ni-rich phase ($0 < y < 1$) according to Ni/P stoichiometric ratio [12]. P-rich phases commonly suffer from complex synthesis conditions, such as high temperature, high pressure, low thermodynamic stability, and short cycle life. By contrast, Ni-rich

✉ Peng Zhang
  jluvip@sina.com

  Wenxian Wang
  wwx960@126.com

  Zimin Kou
  zmkou@163.com

  Jinzhe Li
  18435138298@163.com

  Tao Wang
  tyutwt@163.com

  Jibao Guo
  703836614@qq.com

[1] College of Mechanical and Vehicle Engineering, Taiyuan University of Technology, Taiyuan 030024, People's Republic of China

[2] College of Materials Science and Engineering, Taiyuan University of Technology, Taiyuan 030024, People's Republic of China

[3] Taiyuan Tongze Heavy Industry Co., Ltd, Taiyuan 030024, People's Republic of China

phases represented by Ni_2P presented metallicity and had the advantages of high thermodynamic stability, good electrical conductivity, and good electrochemical performance.

Currently, the main synthesis methods of NiP_y, especially Ni_2P, included hydrothermal/solvothermal methods, low-temperature phosphating, high-energy ball milling method, and chemical vapor deposition method [22–26]. Zhao et al. [27] demonstrated one-step colloid method synthesis Ni_2P nanoplates that process excellent electrochemical performance and high energy density. During the preparation, the reaction mixture, including nickel foam, tri-phenylphosphine, and various organic solvents, was quickly heated to 120 °C and kept for 30 min and then heated to 320 °C (maintained for 2 h in an Ar environment). Afterwards, Xie et al. [28] reported a solid-state reaction method to synthesize $Ni_2P/Ni_{12}P_5$ composite that exhibited an excellent gravimetric capacity of 147.3 mAh g^{-1} at 1 A g^{-1} and impressive capacitance retention. However, the preparation time was up to 4 h including 2 h annealing at 300 °C in N_2 atmosphere and passivation in a 1.0% O_2/N_2 mixture for 2 h. Wang's group [29] synthesized Ni-P precursor by using high-energy mechanical ball milling under an Ar atmosphere. Then, the as-prepared Ni-P precursor was treated by annealing at 300–500 °C for 2 h at different temperatures for the phase transformation, including Ni_2P and Ni_5P_4. Despite numerous research efforts in the synthesis methods of Ni_2P nanosphere and nanosheets, the existing research methods have many drawbacks, such as high heating temperature, prolonged heating, inert gas protection, and tedious preparation procedure [30].

We report a one-step microwave-assisted solvothermal nano-manufacturing method to synthesis phase-pure Ni_2P nanosphere, with rP as the P source and $Ni(NO_3)_2•6H_2O$ as the Ni source. Remarkably, the synthesized method local heating property in the reaction site expedites heat dissipation rate and avoids unwanted phase transition between Ni and P compounds. The method also has the advantages of low energy consumption, fast heating and cooling, and shorter reaction time. The reaction time is only 120 s, which is shorter compared with the 2- to 6-h reaction time in traditional methods; this is due to the properties of fast heating and response facilitation of microwave [31, 32]. Furthermore, the method needs no protective atmosphere and has low requirements in terms of equipment, which is only a household microwave oven. We also studied the influences of microwave power, microwave radiation time, and ratio of Ni/P on the structure and phases of products. The optimum asymmetric supercapacitors showed an outstanding energy density of 27.2 Wh kg^{-1} and power density of 375 W kg^{-1}. This work provided a strategy for the synthesis of phase-pure Ni_2P that is facile and highly efficient with low energy consumption and requires no atmosphere protection; it has significant and wide applications in sodium-ion batteries, electrical catalysis [20], hydrogen evolution reactions, and oxygen evolution reactions, especially in the synthesis of electrode material of high-performance asymmetric supercapacitor.

Experiment

Materials

$Ni(NO_3)_2•6H_2O$, rP, ethylenediamine, ethylene glycol, polytetrafluoretyhylene, carbon black, and active carbon. All chemical reagents in our experiments were purchased from Sinopharm and used without further treatment. Deionized (DI) water was used to prepare all aqueous solutions.

Preparation of Ni₂P

Ni_2P nanosphere was synthesized by a simple one-step microwave method and can be explained as Eq. 1. First, 40 mg of $Ni(NO_3)_2•6H_2O$ and 20 mg of rP were mixed evenly in a mortar. Then, the mixture was dispersed over 400 μL of ethylenediamine and 200 μL of ethylene glycol. Finally, the evenly mixed mixture was transferred to the microwave oven (Panasonic NN-GF362M). Under the condition of 1000 W microwave radiation, black powder was obtained after irradiation for 120 s without any treatment. A series of Ni_2P nanosphere prepared under different conditions are listed in Table 1.

Material characterization

The morphologies of the as-prepared Ni_2P nanosphere were observed by field emission scanning electron microscopy (FESEM, HITACHI-SU8010) and energy dispersive X-ray spectroscopy (EDS). The crystalline structure and elemental valence states of Ni_2P nanosphere were characterized by X-ray powder diffraction (XRD, PANalytical, X'Pert-PRO MPD, Netherlands) and X-ray photoelectron spectroscopy (XPS, ESCALAB 250 XPS System, Thermo Fisher Scientific, UK).

Electrochemical characterization

For the electrochemical tests of the Ni_2P nanosphere, the as-prepared polytetrafluoretyhylene (10 wt%), carbon black (10 wt%) and active materials (80 wt%) were coated on a nickel foam (1×1 cm^2) and dried in 80 °C of oven for 12 h. In the three-electrode system, platinum (Pt) foil was used as counterelectrode, and Hg/HgO (RO501) electrode was used as reference electrode. The asymmetric supercapacitors cell was manufactured by using the active carbon as a negative electrode and Ni_2P nanosphere as positive electrode. In this work, the specific capacitance (C, F g^{-1}), energy density (E,

Table 1 Operation conditions for synthesizing Ni$_2$P nanosphere

Material	Ni:P	Ni (mg)	Ni (mol/L)	P (mg)	P (mol/L)	Microwave power (W)	Heating time (s)
R1	30:15	30	0.172	15	0.807	1000	120
R2	40:20	40	0.229	20	1.076	1000	120
R3	50:25	50	0.287	25	1.345	1000	120
P1	40:20	40	0.229	20	1.076	800	120
T1	40:20	40	0.229	20	1.076	1000	60
T2	40:20	40	0.229	20	1.076	1000	180

Ni Ni(NO$_3$)$_2$•6H$_2$O, *P* red phosphorus

Wh kg^{-1}), and power density (*P*, kW kg^{-1}) are calculated according to the following formulas [33, 34]:

$$C = (I \times \Delta t)/(\Delta V \times m) \tag{1}$$

$$E = C\Delta V^2/(2 \times 3.6) \tag{2}$$

$$P = 3600 \times E/\Delta t \tag{3}$$

In these formulas, $\triangle t$ is discharge time (s), $\triangle v$ is the potential range (V), *I* is the current (A), and *m* is the mass of active material (mg). The electrochemical performances which galvanostatic-charge-discharge (GCD), electrochemical impedance spectroscopy (EIS), and cyclic voltammetry (CV) were tested by electrochemical workstation (Chenhua, CHI 760E).

The asymmetric supercapacitors are 6 M KOH as electrolyte, the cathode materials and anode materials are Ni$_2$P nanospheres and activated carbon (AC), respectively. Among them, the optimal mass ratio of cathode and anode electrodes materials is calculated by the following equation, where *m* (g), *C* (F g^{-1}), and ΔV (V) represent the mass of active materials, specific capacitance, and discharge voltage, respectively. The mass ratio of positive and negative materials is maintained at 1.1.

$$m^+/m^- = C^-\Delta V^-/C^+\Delta V^+ \tag{4}$$

Results and discussion

Synthesis mechanism and characterization

In this work, we report our discovery of a facile and energy-efficient method with multi-scale aggregation dynamics for the microwave-assisted synthesis of Ni$_2$P nanospheres. Our technique represents a clean and ultrafast (120 s) nano-manufacturing approach that uses microwave heating without any inert gas protection and intense facilities. Scheme 1 supplies the schematic of our hypothesized mechanism of the process. Microwave heating-initiated reaction between Ni(NO$_3$)$_2$•6H$_2$O and red phosphorus. This reaction results in the synthesis of Ni$_2$P nanospheres, with Ni(NO$_3$)$_2$•6H$_2$O providing the precursor. These nanospheres undergo fierce heating, which promotes molecular collisions and the formation of aggregates. In the first stage of aggregation, the nanosphere sizes generated by the reaction were too small (approximately few nanometers). The van der Waals (vdW) interactions then governed the aggregation of particles, resulting in the spherical growth of the aggregate (~80 nm). The second stage of aggregation involves particles with much larger diameters (~50 μm), and the difference in each surface energies (nanosphere-solution and nanosphere-nanosphere) became dominant, resulting in the directional growth of the aggregate. This phenomenon led to a block-like growth of Ni$_2$P aggregates (Fig. 3b).

Figure 1 displays the X-ray diffraction (XRD) patterns of samples using different synthesis parameters of feed ratio (ratio of solute and solvent), microwave power, and heating time based on the one-step microwave-assisted solvothermal nanomanufacturing method. As shown in the illustration, the synthesis parameters play important roles in the quantity and crystallinity of Ni$_2$P, as well as residues of reactants. In the case of sample R1, R2, P1, and T2, the well-defined Bragg diffraction peaks at $2\theta = 17.5°, 30.5°, 31.8°, 35.3°, 40.7°, 44.6°, 47.3°, 54.2°, 54.9°, 66.2°, 72.7°$, and $74.8°$ were consistent with characteristic diffraction patterns of Ni$_2$P (JCPDS-074-1385), respectively, and no characteristic peaks of other Ni/P phases existed. By contrast, the sample R2 corresponding to 0.229 mol/L of Ni(NO$_3$)$_2$•6H$_2$O and 1.076 mol/L of rP shown in Table 1 possessed relatively higher and narrower diffraction peaks and fewer peaks of other substances than other samples. Ni$_2$P nanoparticles with good crystallinity were obtained under R2 reaction conditions. At the same time, obvious residual admixtures of the orthorhombic system rP (JCPDS-076-1957) and triclinic system Ni(NO$_3$)$_2$•4H$_2$O (JCPDS-74-0666) were observed in diffraction patterns of sample R3 and T1, as well as weak peaks of Ni$_2$P. The possible reason for this is that the quantity of heat transmitted by quantitative solvent is fixed in unit time, both excessive sources of Ni (Ni(NO$_3$)$_2$•6H$_2$O and P (rP) in sample R3 and
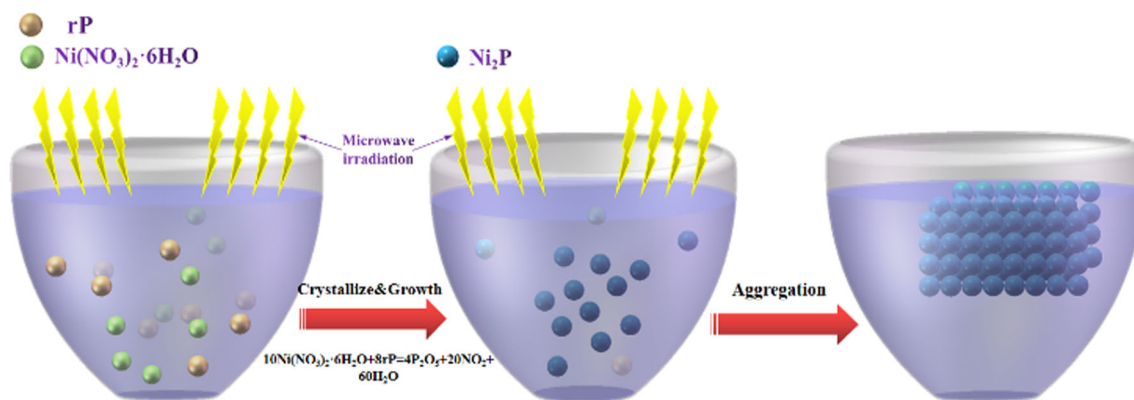
Scheme 1 The synthesis process of one-step microwave-assisted solvothermal for the phase-pure Ni₂P.

less reaction time 60 s in sample T1 had significant effects on the energy absorption of reaction systems and resulted in insufficient driving force for the reaction.

To further explore the composition of prepared materials from sample R2, an attempt was carried out to access the binding energy and chemical states of the bonded elements through X-ray photoelectron spectroscopy (XPS) analyses. The high-resolution spectrum of Ni 2p exhibited in Fig. 2a contained two sets of peaks ascribed to different Ni species and multi-electron excitation. Each set of peaks included two dominating peaks corresponding to Ni (2p3/2) and Ni (2p1/2) and a satellite peak. Two main peaks centered at 853.1 and 869.2 eV were associated with the Ni (2p3/2) and Ni (2p1/2), respectively, which are attributed to the Ni-P of Ni₂P. Two main peaks centered at 856.0 and 873.7 eV were assigned to the Ni (2p3/2) and Ni (2p1/2), respectively, which were attributed to the Ni-O. The bands noted at 861.7 and 880.1 eV

related to satellite peaks. The high-resolution spectrum of P 2p, as shown in Fig. 2b, possessed two peaks centered at 129.1 and 129.8 eV, which were assigned to the binding energy of P (2p3/2) and P (2p1/2) of P-Ni, respectively. One remarkable peak centered at 133.4 eV demonstrated the oxidation state of P, which can be ascribed to oxidized P species generated on the surface of Ni₂P nanoparticles resulting from exposure to air during XPS measurement. The XPS results clearly demonstrated that the composite was that of Ni-P, which is consistent with the XRD result.

The influences of different reaction conditions, including qualities of Ni(NO₃)₂•6H₂O and rP, microwave power, and reaction time, on the characteristic and morphology of resultants have been investigated by SEM analyses, whereas the mass of solvents including ethylenediamine and ethylene glycol, as well as molar ratio of Ni(NO₃)₂•6H₂O and rP, remained constant under all synthesis conditions. The reactant system absorbed

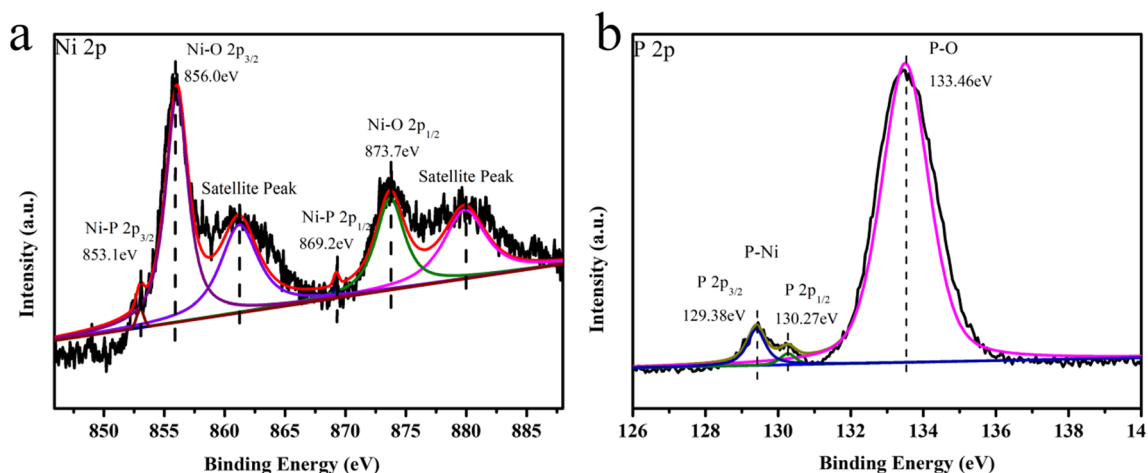**Fig. 1** The XRD pattern of Ni₂P synthesized by different operation conditions
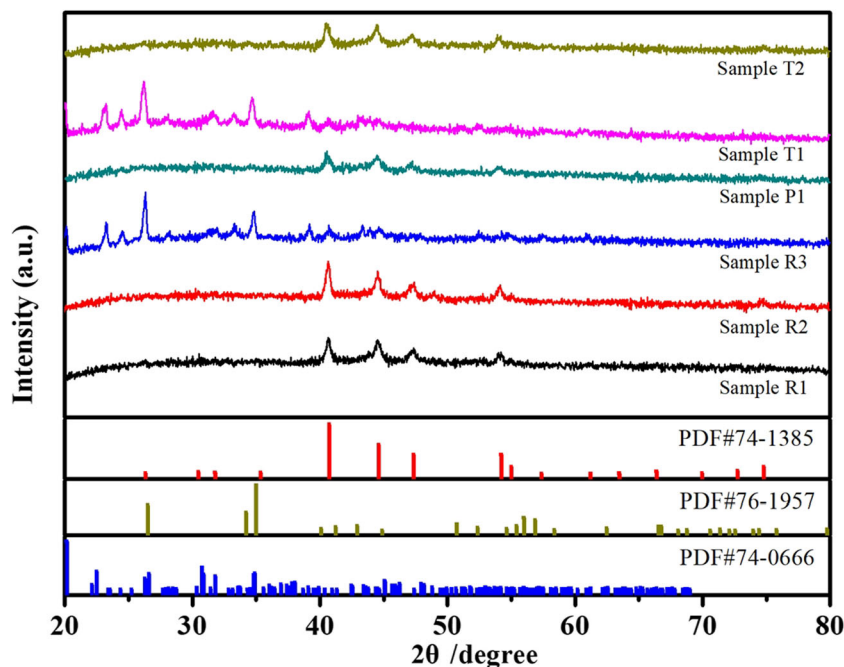
Fig. 2 The XPS spectra of sample R2: **a** Ni 2p and **b** P 2p

equal heat in unit time when the microwave power was fixed due to the mass of solvents kept constant. As illustrated in Fig. 3b and the high magnification in Fig. 3c and f, uniform spherical

particles with an average diameter of 80 nm were formed under the condition R2. This phenomenon occurs because the organic solvent transfers a large amount of heat to drive the reaction, and
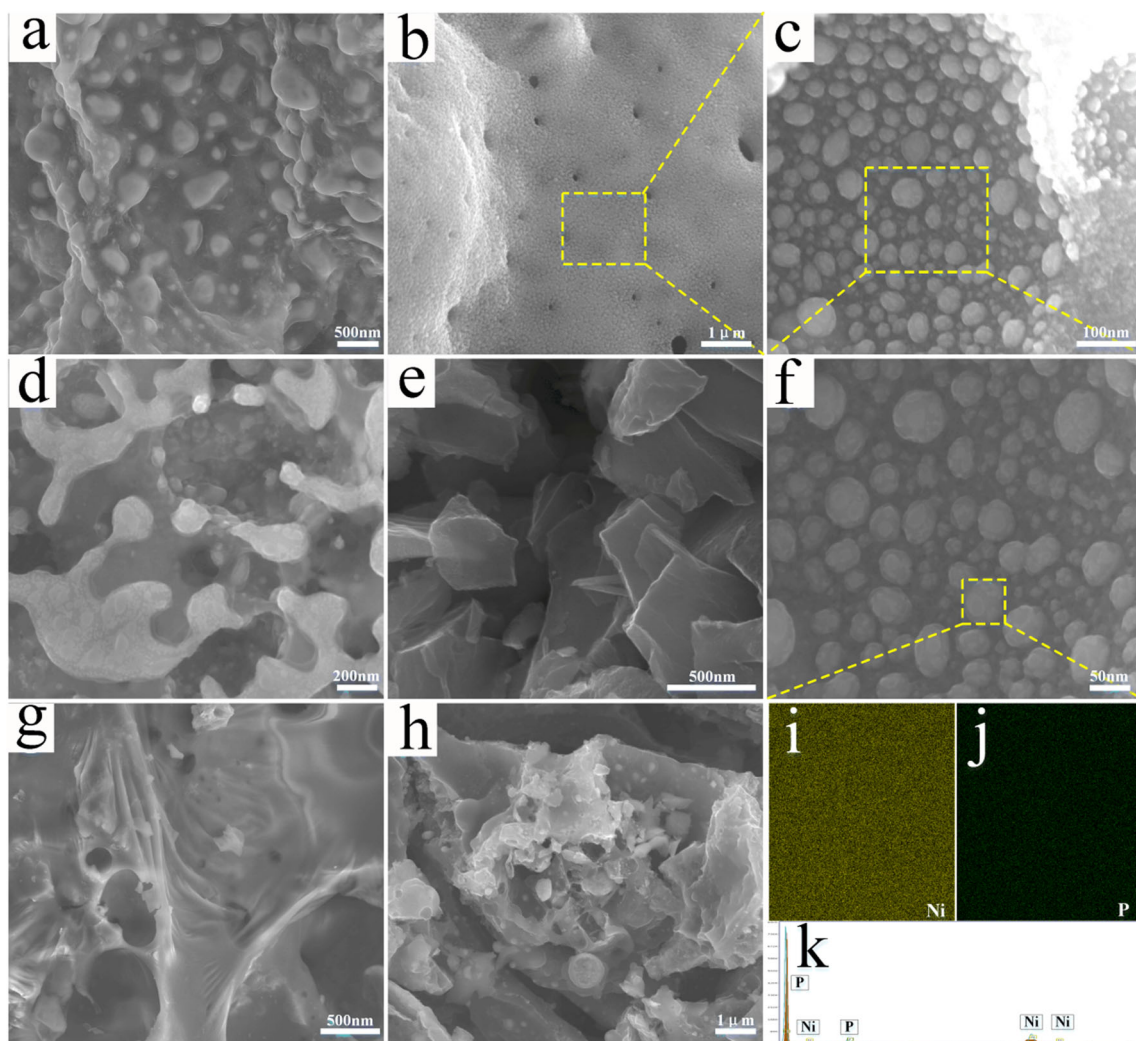

Fig. 3 **a–h** High magnification of SEM images (**a** sample R1; **b**, **c** and **f** sample R2; **d** sample R3; **e** sample P1; **g** sample T1; **h** sample T2) of Ni_2P, and **i–k** corresponding Ni and P elemental mapping of Ni_2P

then because of the van der Waals interaction, the particles tend to gather together to crystallize and form nanoparticles. Figure 3a shows the SEM image of sample R1, which it can be seen that excessive microwave energy absorbed by the solvent is not conducive to the formation of Ni_2P nanospheres. Conversely, when the precursor was present in excess (Fig. 3d), the microwave energy absorbed by the reactants was not sufficient for the complete reaction (sample R3), and there were still some unreacted precursors in the products. Therefore, fewer Ni_2P nanoparticles were generated, which was also confirmed in the XRD pattern. Similarly, as shown in Fig. 3e (sample P1, the microwave power is too low), and the heat absorbed by the solvent is not enough to decompose the precursor, so the complete Ni_2P nanospheres cannot be formed. This is due to the fact that the lower microwave power meant that less energy could be delivered to reactants, which meant that insufficient energy was present to drive the crystallization and formation of spherical nanoparticles. Figure 3g (sample T1) presents a bulk organization instead of spherical nanoparticles, because the microwave duration time was too short for reaction and crystallization. As shown in Fig. 3h (Sample T2), the nanoparticles agglomerated, because the excess microwave energy forced the particles to collide and gather [35]. To further illustrate the composition of nanoparticles, the corresponding EDS spectra of the Ni_2P nanoparticles are shown in Fig. 3i–k, where C, P, and Ni elements are displayed. Considering the abovementioned analysis, the preparation condition according to sample R2 was optimal and recommended.

As shown in the low-magnification TEM (Fig. S1a), it can be obviously observed that Ni_2P nanospheres is basically consistent with the SEM results. According to HRTEM figure, the planar spacing of well-defined lattice stripes is 0.22 nm, which is consistent with the spacing of (111) crystals, and is a hexagonal Ni_2P plane. The electron diffraction (SAED) pattern in the selected region is shown in the inset of Fig. S1b. Diffraction rings correspond to nanoparticles.

Electrochemical performance

Electrochemical properties in a three-electrode system

To obtain the optimal ratio of raw materials ($Ni(NO_3)_2$•$6H_2O$: P and reaction conditions (microwave power and time), we conducted an investigation under the abovementioned conditions, as shown in Table 1. The electrochemical properties of Ni_2P nanosphere were conducted to evaluate in 6.0 M KOH aqueous electrolyte.

Figure 4 a shows that when the input amount of raw materials was appropriately increased, the specific capacitance of the material was relatively higher, because the solvent absorbed microwave energy and generated a large amount of heat to accelerate the decomposition of raw materials. When the precursor content is too low, the target product will be generated, but part of the excess energy will lead to large-scale agglomeration of electrode materials, which is not conducive to the electron transfer and therefore the energy storage. However, the introduction of too many raw materials led to insufficient heat absorption and incomplete reaction, thereby leading to the reduction of the specific capacitance. The optimal raw material content was 0.229 mol/L of $Ni(NO_3)_2$•$6H_2O$ and 1.076 mol/L phosphorus (sample R2). Figure 4b and c shows the effect of microwave power and reaction time on the capacitance. Low power (800 W) and short time (60 s) can lead to a lack of microwave energy, which may produce non-ideal forms and incomplete reactions. For example, as shown from the XRD pattern, due to the short reaction time, some unreacted phosphor powder existed. However, as time went on (180 s), microwave energy caused the nanosphere to aggregate. In summary, the best reaction conditions of the nanosphere are mass ratio ($Ni(NO_3)_2$•$6H_2O$: P) of 20:40, a microwave time of 120 s, and a power of 1,000 W.

In order to further clarify the electrochemical properties of the Ni_2P nanosphere (material R2), we performed a series of electrochemical experiments. The GCD curves of Ni_2P nanosphere electrodes (Fig. 5a) show nonlinear charge/discharge curves with a clear platform, which explain the electrodes materials excellent faradaic capacitance behavior [36]. At the same current density, the discharge time of material R2 electrode is longer than that of other materials, which may be due to the good morphology a providing reaction sites for electron transfer, which is conducive to the energy storage reaction. Afterwards, the electrochemical properties of the sample (R2) under the best preparation conditions were tested as show in Fig. 5b–f. Figure 5b shows the CV curves of the Ni_2P nanosphere at potential scan rates ranging from 2.5–100 mV s^{-1}. The clear redox peak on the CV curve indicates
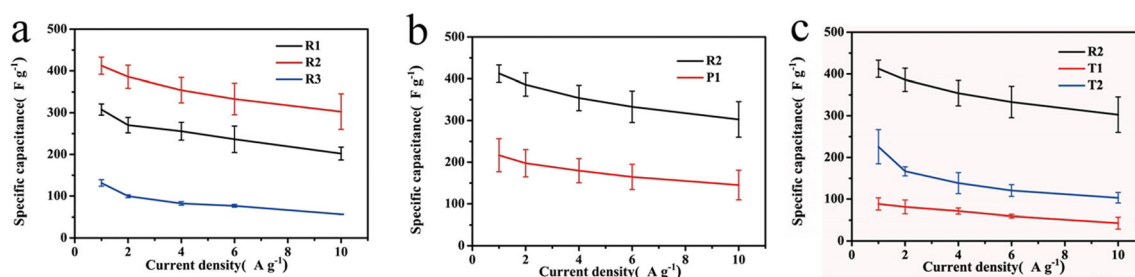

Fig. 4 Specific capacitance of Ni_2P nanosphere with different **a** feeding ratios, **b** contents of microwave power, and **c** reaction time
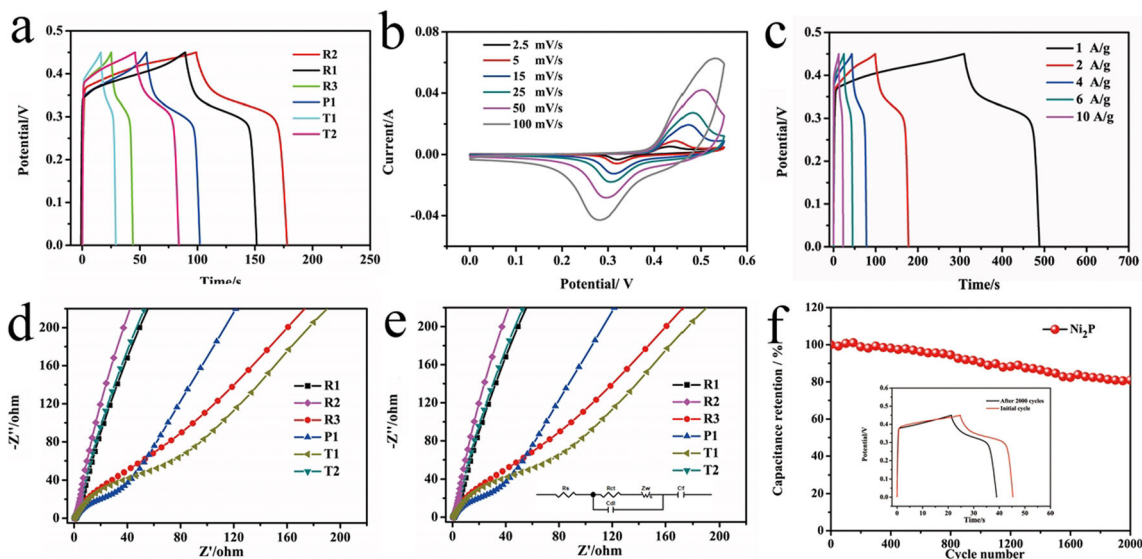
Fig.5 a GCD curves of Ni$_2$P nanosphere electrode materials with different preparation condition current density of 2 A g^{-1}; **b** CV curves of Ni$_2$P nanosphere electrode material (R2) at different scan rates; **c** GCD curves of Ni$_2$P nanosphere material (R2) at different current density; **d** Nyquist plots of Ni$_2$P nanosphere electrode materials with different preparation condition at low frequency; **e** Nyquist plots at high frequency; **f** cycling stability of Ni$_2$P nanosphere electrode materials at 6 A g^{-1} and GCD curves at initial cycle and after 2000 cycles (inset)

the typical battery-type electrochemical behavior of the electrode material. The charge/discharge curves of Ni$_2$P nanosphere electrodes exhibit outstanding special capacitance of 404.2, 362.6, 332.7, 304.3, and 287 F g^{-1} at the rates of 1, 2, 4, 6, and 10 A g^{-1}, respectively. Moreover, the redox process of Ni$_2$P in KOH electrolyte as follow [37]:

$$Ni_2P + 2OH^- \leftrightarrow Ni_2P(OH)_2 + 2e^- \tag{5}$$
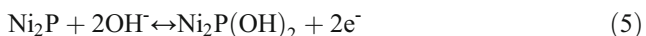
In Fig. 5d, e, the Nyquist plots curves (R2) of low frequency were nearly vertical, representing their nearly ideal capacitance behaviors. Compared with other electrode materials, R2 had a faster kinetic conduction rate, which was due to its special spherical structure, making the diffusion path of the ions shorter and making diffusion inside and outside the electrode easier. The interface resistance, electronic resistance of the electrode materials, and ionic resistance of the electrolytes can be represented by the equivalent series resistance (Rs), which reflected the intercept on the real axis of the figure. The Rs of the Ni$_2$P nanosphere material was around 0.62 Ω, which showed lower resistance than other materials, indicating that the electrode material had low internal resistance. The diameter of the semicircle was used to define the charge transfer resistance (Rct) of the redox reactions at the electrode/electrolyte surface, and the Rct for Ni$_2$P nanosphere was lower than the other materials. It is noteworthy that the Ni$_2$P nanosphere shows 81% retention of initial specific capacitance after 2000 cycles. According to the GCD cures of Ni$_2$P nanosphere (Fig. 5f inset) after the cyclic test, the two shoulder-shaped platforms of the charge-discharge curve only slightly shifted due to the oxidation reaction, indicating that the material had excellent cycling stability.

The processes of Faraday reaction of redox species and ion diffusion in the electrode material/electrolyte are the pathways of capacitance generation in an electrode material. The total capacitance of the electrode material is composed of the following two parts: (1) the capacitance behavior is generated by ion adsorption/desorption and REDOX reactions, independent of current density and scanning rate. (2) The diffusion process, which was caused by ion insertion into both the electrode material and electrolyte. The contribution to the capacitance of different processes can be calculated by the following formula [38, 39]:

$$i = kv + k'v^{0.5} \tag{6}$$

where i is the current, and k and k' are constants. Figure 6 a shows the capacitive contribution (shaded region) of Ni$_2$P nanosphere at the scan rate of 50 mV s^{-1}. Figure 6 b shows the capacitive contribution increasing with decreasing scan rate. This result proved that good rate capability is inseparable from material capacitive contribution. In Fig. 3c, the relationship between peak current (i) and sweep rate (v) is as follows [[40, 41]]:

$$i = av^b \tag{7}$$

where a and b are adjustable values. The value of b depends on the slope of the line in Fig. 6c. When $b = 0.5$, the capacitance is contributed by diffusion. Similarly, when $b = 1$, the capacitance is contribution by capacitive processes. Figure 6 c shows that the slope of the anode peak is 0.6773, and the slope of the cathode peak is 0.6943 for the Ni$_2$P nanosphere, demonstrating a common capacitive behavior.
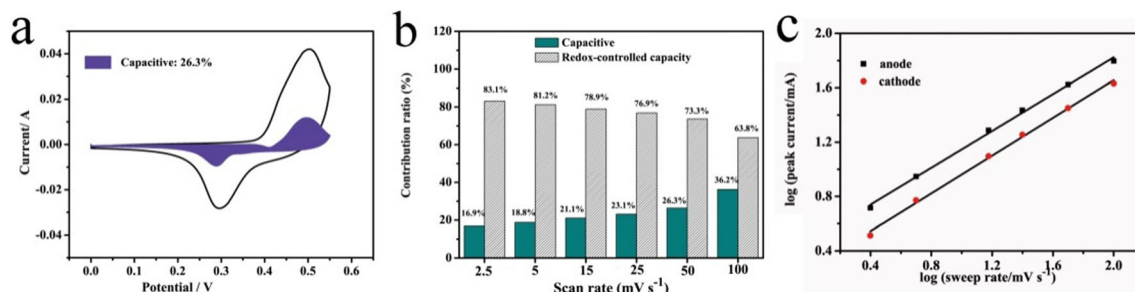
Fig.6 **a** CV profile showing the capacitive and diffusion contribution of Ni$_2$P nanosphere (R2) at 50 mV s^{-1}; **b** capacitive and diffusion contribution to the total capacity at different scan rates; **c** relationship of the square root of scan rate and the peak current density

Electrochemical characterization for the assembled ASCs

To estimate the electrochemical property of Ni$_2$P//AC cell, the CV curves were conducted with a two-electrode device at different scan rates (Fig. 7a). Combined with the galvanostatic charge-discharge curve in Fig. 7b, we found that the position of the redox peak in the CV curve corresponded to that of the charge-discharge platform. As shown in Fig. 7c, the GCD curves of Ni$_2$P//AC cell at different voltages were also between 1.2 and 1.6 v. The galvanostatic charging and discharging processes take the same time, which indicated that the device had strong electrochemical reversibility [42]. Figure 7 d exhibits the Nyquist plots of Ni$_2$P//AC cell, and the inset demonstrates the high-frequency region. Figure 7 e shows that electrolyte ions can be diffused and transported promptly in the cell. The curve deviates from the X-axis in the low-frequency region, indicating that the material has high conductivity. According to the GCD curves, the specific capacitance values were calculated as 87.1, 71.4, 61.8, 45.8, and 36.5 F g^{-1} (27.2, 22.3, 19.9, 14.3, and 11.4 kW kg^{-1}) at current densities of 0.5, 1, 2, 3, and 5 A g^{-1}, respectively. In Fig. 7g, the Ni$_2$P//AC shows exceptional cycling stability, with 86.6% of its initial capacitance retained after 5000 cycles at a current density of 3 A g^{-1}. To test the asymmetric

supercapacitor, commercial LEDs were powered using the assembled device. The device can light up five LEDs for over 8 min, indicating excellent energy storage ability and large output power. The self-discharge (SD) characteristics are key factors for the evaluation of possible commercial and overall property viability in the device. Here, Ni$_2$P//AC cell was charged to the maximum voltage of 1.4 V and held at the potential self-discharge for 10 h. According to the diagram analysis (Fig. 7h), the voltage decreased significantly in the first stage and then gradually stabilized at around 1.05 V. This phenomenon, as explained by Chen et al., is due to the decomposition of water as a solvent in the initial stage of self-discharge of the device; thus, the battery voltage drops rapidly [43].

Conclusion

Ni$_2$P nanospheres were successfully fabricated by microwave-assisted solvothermal method. This method had the advantages of short reaction time and requiring no post-treatment and gas protection. Ni$_2$P nanosphere exhibited a superior specific capacitance of 404.2 F g^{-1} at 1 A g^{-1} and excellent cycling stability (retaining 81% after 2000 cycles at 6 A
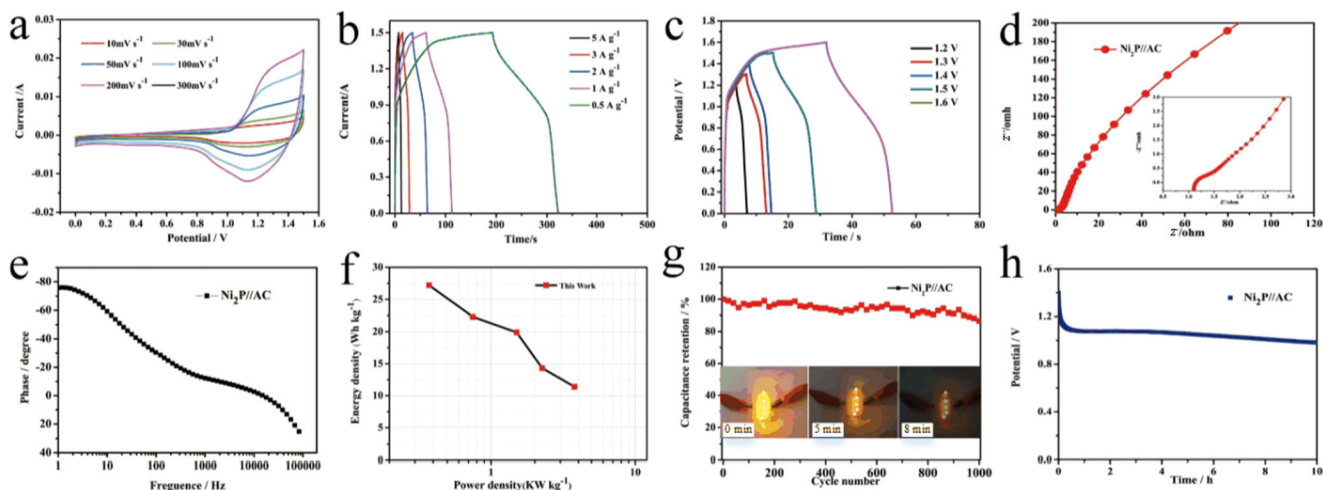

Fig.7 **a** CV curves of Ni$_2$P//AC at different scan rates; **b** GCD curves of Ni$_2$P//AC with different current densities; **c** the GCD curves at different potentials; **d** Nyquist plots of Ni$_2$P//AC at low frequency and high frequency (inset); **e** Nyquist plots of Ni$_2$P//AC; **f** Ragone plots of the Ni$_2$P//AC cell; **g** cycling stability of Ni$_2$P//AC; (e) self-discharge curves of the device

g^{-1}). When applied as a Ni_2P nanosphere anode material, the optimum device showed an outstanding energy density of 27.2 Wh kg^{-1} and power density of 375 W kg^{-1}, and this energy storage device can light three small LED light bulbs for 6 min. In addition, the discovery of this new technique for synthesis transition metal phosphide will accelerate substantial progress toward more widespread use of synthesis transition metal phosphide through more energy-efficient and easily available methods.

Compliance with ethical standards

Conflict of interest The authors declare that they have no conflict of interest.

References

1. Yang L, Lu XT, Wang SH, Wang JS, Guan XH, GuanX WGS (2020) Designed synthesis of nickel-cobalt-based electrode materials for high-performance solid-state hybrid supercapacitors. Nanoscale 12:1921–1938

2. Yang L, Yang Y, Wang SH, Guan XH, Guan X, Wang GS (2020) Multi-heteroatom-doped carbon materials for solid-state hybrid Supercapacitors with a Superhigh cycling performance. Energ Fuel 34:5032–5043

3. Guan XH, Huang M, Yang L, Wang GS, Guan X (2019) Facial design and synthesis of CoSx/Ni-co LDH nanocages with rhombic dodecahedral structure for high-performance asymmetric supercapacitors. Chem Eng J 372:151–162

4. Jing C, Liu XL, Liu XY, Jiang DB, Dong BQ, Dong F, Wang JS, Li N, Lan T, Zhang YX (2018) Crystal morphology evolution of Ni-co layered double hydroxide nanostructure towards high-performance biotemplate asymmetric supercapacitors. Crystengcomm 20:7428–7434

5. Zhu YR, Wu ZB, Jing MJ, Hou HS, Yang YC, Zhang Y, Yang XM, Song WX, Jia XN, Ji XB (2015) Porous $NiCo_2O_4$ spheres tuned through carbon quantum dots utilised as advanced materials for an asymmetric supercapacitor. J Mater Chem A 3:866–877

6. Sun HH, Ma Z, Qiu YF, Liu H, Gao GG (2018) Ni@NiO nanowires on nickel foam prepared via "acid hungry" strategy: high supercapacitor performance and robust electrocatalysts for water splitting reaction. Small 14:1800294

7. Wang YP, Pan AQ, Zhang YF, Shi JR, Lin JD, Liang SQ, Cao GZ (2018) Heterogeneous NiS/NiO multi-shelled hollow microspheres with enhanced electrochemical performances for hybrid-type asymmetric supercapacitors. J Mater Chem A 6:9153–9160

8. Seo DH, Pineda S, Yick S, Bell J, Han ZJ, Ostrikov K (2015) Plasma-enabled sustainable elemental lifecycles: honeycomb-derived graphenes for next-generation biosensors and supercapacitors. Green Chem 17:2164–2171

9. Wang XJ, Chen K, Wang G, Liu XJ, Wang H (2017) Rational design of three-dimensional graphene encapsulated with hollow FeP@carbon nanocomposite as outstanding anode material for Lithium ion and sodium ion batteries. ACS Nano 11:11602–11616

10. Li ZQ, Zhang LY, Ge XL, Li CX, Dong SH, Wang CX, Yin LW (2017) Core-shell structured CoP/FeP porous microcubes interconnected by reduced graphene oxide as high performance anodes for sodium ion batteries. Nano Energy 32:494–502

11. Zhu PP, Zhang Z, Hao SJ, Zhang BW, Zhao PF, Yu J, Cai JX, Huang YZ, Yang ZY (2018) Multi-channel FeP@C octahedra anchored on reduced graphene oxide nanosheet with efficient performance for lithium-ion batteries. Carbon 139:477–485

12. Lou PL, Cui ZH, Jia ZQ, Sun JY, Tan YB, Guo XX (2017) Monodispersed carbon-coated cubic NiP_2 nanoparticles anchored on carbon nanotubes as ultra-long-life anodes for reversible Lithium storage. ACS Nano 11:3705–3715

13. Bai YJ, Zhang HJ, Fang L, Liu L, Qiu HJ, Wang Y (2015) Novel peapod array of Ni_2P@graphitized carbon fiber composites growing on Ti substrate: a superior material for Li-ion batteries and the hydrogen evolution reaction. J Mater Chem A 3:5434–5441

14. Elshahawy AM, Guan C, Li X, Zhang H, Hu YT, Wu HJ, Pennycook SJ, Wang J (2017) Sulfur-doped cobalt phosphide nanotube arrays for highly stable hybrid supercapacitor. Nano Energy 39:162–171

15. Pan Y, Chen YJ, Lin Y, Cui PX, Sun KA, Liu YQ, Liu CG (2016) Cobalt nickel phosphide nanoparticles decorated carbon nanotubes as advanced hybrid catalyst for hydrogen evolution. J Mater Chem A 4:14675–14686

16. Huang C, Pi CR, Zhang XM, Ding K, Qin P, Fu JJ, Peng X, Gao B, Chu PK, Huo KF (2018) In situ synthesis of MoP nanoflakes intercalated N-doped graphene nanobelts from MoO_3-amine hybrid for high-efficient hydrogen evolution reaction. Small 14:1800667

17. Xu YL, Peng B, Mulder FM (2018) A high-rate and Ultrastable sodium ion anode based on a novel Sn_4P_3-P@Graphene nanocomposite. Adv Energy Mater 8:1701847

18. Liu S, Sankar KV, Kundu A, Ma M, Kwon JY, Jun SC (2017) Honeycomb-like interconnected network of nickel phosphide Heteronanoparticles with superior electrochemical performance for Supercapacitors. ACS Appl Mater Interfaces 9:21829–21838

19. Shi SS, Li ZP, Sun Y, Wang B, Liu QN, Hou YL, Huang SF, Huang JY, Zhao YF (2018) A covalent Heterostructure of Monodisperse Ni_2P immobilized on N, P-co-doped carbon nanosheets for high performance sodium/lithium storage. Nano Energy 48:510–517

20. Ni YH, Jin LN, Hong JM (2011) Phase-controllable synthesis of nanosized nickel phosphides and comparison of photocatalytic degradation ability. Nanoscale 3:196–200

21. Li H, Xu SM, Yan H, Yang L, Xu SL (2018) Cobalt phosphide composite encapsulated within N,P-doped carbon nanotubes for synergistic oxygen evolution. Small 14:1800367

22. Zhao Q, Han Y, Huang X, Dai JH, Tian JT, Zhu ZB, Yue L (2017) Hydrothermal synthesis of Ni_2P nanoparticle and its hydrodesulfurization of dibenzothiophene. J Nanopart Res 19:123

23. Zhou K, Zhou WJ, Yang LJ, Lu J, Cheng S, Mai WJ, Tang ZH, Li LG, Chen SW (2015) Ultrahigh-performance pseudocapacitor electrodes based on transition metal phosphide nanosheets array via phosphorization: a general and effective approach. Adv Funct Mater 25:7530–7538

24. An CH, Wang YJ, Li L, Qiu FY, Xu YN, Xu CC, Huang YN, Jiao F, Yuan HT (2014) Effects of highly crumpled graphene nanosheets on the electrochemical performances of pseudocapacitor electrode materials. Electrochim Acta 133:180–187

25. Ji JY, Zhang LL, Ji HX, Li Y, Zhao X, Bai X, Fan XB, Zhang FB, Ruoff RS (2013) Nanoporous Ni $(OH)_2$ thin film on 3D ultrathin-graphite foam for asymmetric Supercapacitor. ACS Nano 7:6237–6243

26. Parveen N, Hilal M, Han JI (2020) Newly design porous/sponge red phosphorus@graphene and highly conductive Ni_2P electrode for

asymmetric solid state Supercapacitive device with excellent performance. Nano-Micro Lett 12:25

27. Zhao Y, Zhao M, Ding X, Liu ZR, Tian H, Shen HH, Zu XT, Li SA, Qiao L (2019) One-step colloid fabrication of nickel phosphides nanoplate/nickel foam hybrid electrode for high-performance asymmetric supercapacitors. Chem Eng J 373:1132–1143

28. Xie SL, Gou JX (2017) Facile synthesis of $Ni_2P/Ni1_2P_5$ composite as long-life electrode material for hybrid supercapacitor. J Alloy Compd 713:10–17

29. Wang D, Kong LB, Liu MC, Luo YC, Kang L (2015) An approach to preparing Ni-P with different phases for use as supercapacitor electrode materials. Chem-Eur J 21:17897–17903

30. Wang D, Kong LB, Liu MC, Luo YC, Kang L (2015) An approach to preparing Ni-P with different phases for use as supercapacitor electrode materials. Chem-Eur J 21:17897–17903

31. Bi YH, Nautiyal A, Zhang HP, Luo JJ, Zhang XY (2018) One-pot microwave synthesis of NiO/MnO_2 composite as a high-performance electrode material for supercapacitors. Electrochim Acta 260:952–958

32. Bi YH, Nautiyal A, Zhang HP, Yan H, Luo JJ, Zhang XY (2018) Facile and ultrafast solid-state microwave approach to MnO_2-NW@graphite nanocomposites for supercapacitors. Ceram Int 44:5402–5410

33. Zhang L, Du WY, Nautiyal A, Liu Z, Zhang XY (2018) Recent progress on nanostructured conducting polymers and composites: synthesis, application and future aspects. Sci China-Mater 61:303–352

34. Mai LQ, Minhas-Khan A, Tian XC, Hercule KM, Zhao YL, Lin X, Xu X (2013) Synergistic interaction between redox-active electrolyte and binder-free functionalized carbon for ultrahigh supercapacitor performance. Nat Commun 4:2923

35. Wang SM, Guo QP, Liang SJ, Li P, Luo JJ (2018) Preparation of Ni-MOF-74/SBS mixed matrix membranes and its application of CH_4/N_2 separation. Sep Purif Technol 199:206–213

36. Yu L, Zhang L, Wu HB, Lou XW (2014) Formation of NixCo3-xS4 hollow nanoprisms with enhanced pseudocapacitive properties. Angew Chem-Int Edit 53:3711–3714

37. Hou SJ, Xu XT, Wang M, Xu YQ, Lu T, Yao YF, Pan LK (2017) Carbon-incorporated Janus-type Ni_2P/Ni hollow spheres for high performance hybrid supercapacitors. J Mater Chem A 5:19054–19061

38. Xu YL, Peng B, Mulder FM (2018) A high-rate and Ultrastable sodium ion anode based on a novel Sn_4P_3-P@Graphene Nanocomposite. Adv Energy Mater 8:1701847

39. Yin YY, Fan LS, Zhang Y, Liu NN, Zhang NQ, Sun KN (2019) MoP hollow nanospheres encapsulated in 3D reduced graphene oxide networks as high rate and ultralong cycle performance anodes for sodium-ion batteries. Nanoscale 11:7129–7134

40. Lou PL, Cui ZH, Jia ZQ, Sun JY, Tan YB, Guo XX (2017) Monodispersed carbon-coated cubic NiP_2 nanoparticles anchored on carbon nanotubes as ultra-long-life anodes for reversible Lithium storage. ACS Nano 11:3705–3715

41. Sun L, Zhang Y, Zhang DY, Zhang YH (2017) Amorphous red phosphorus nanosheets anchored on graphene layers as high performance anodes for lithium ion batteries. Nanoscale 9:18552–18560

42. Tian YR, Du HS, Zhang MM, Zheng YY, Guo QP, Zhang HP, Luo JJ, Zhang XY (2019) Microwave synthesis of MoS_2/MoO_2@CNT nanocomposites with excellent cycle stability for supercapacitor electrodes. J Mater Chem C 7:9545–9555

43. Chen LB, Bai H, Huang ZF, Li L (2014) Mechanism investigation and suppression of self-discharge in active electrolyte enhanced supercapacitors. Energy Environ Sci 7:1750–1759